Charge density wave and metallic state coexistence in the multiband conductor TTF[Ni(dmit)$_2$]$_2$

W. Kaddour,[1,2] P. Auban-Senzier,[1] H. Raffy,[1] M. Monteverde,[1] J.-P. Pouget,[1] C. R. Pasquier,[1] P. Alemany,[3] E. Canadell,[4] and L. Valade[5]

[1]*Laboratoire de Physique des Solides, UMR 8502-CNRS, Université Paris-Sud, F-91405 Orsay, France*

[2]*Laboratoire de Physique de la Matière Condensée, Campus Universitaire, Université de Tunis El-Manar, 2092 Tunis, Tunisia*

[3]*Departament de Química Física and Institut de Química Teòrica i Computacional (IQTCUB), Universitat de Barcelona, Martí i Franquès 1, 08028 Barcelona, Spain*

[4]*Institut de Ciència de Materials de Barcelona (CSIC), Campus UAB, 08193 Bellaterra, Spain*

[5]*Laboratoire de Chimie de Coordination, Route de Narbonne, F-31077 Toulouse, France*

(Received 3 May 2014; revised manuscript received 14 August 2014; published 20 November 2014)

We have established a pressure-temperature phase diagram of TTF[Ni(dmit)$_2$]$_2$ based on spin susceptibility at ambient pressure as well as longitudinal and transverse resistivity measurements under pressure up to 30 kbar. The data were analyzed on the basis of first-principles density functional theory calculations. We were able to find several phase transitions and identify three different charge density wave (CDW) states which all coexist with a metallic state in a wide temperature range and superconductivity at the lowest temperatures. This metallicity arises from the development, upon cooling, of a two-dimensional band associated to the Ni(dmit)$_2$ chains. At low pressure, two successive CDW transitions have been clearly identified and are associated to the successive nesting of two strongly one-dimensional bands: The LUMO and HOMO$_1$ of the Ni(dmit)$_2$ chains. These two transitions merge into a single one at 12 kbar which probably corresponds to the partial nesting of a bunch of LUMOs into the HOMO$_1$'s. A maximum of this unique CDW transition temperature is observed at 19 kbar. The CDW instability associated to the LUMO band is announced by an important regime of Peierls-like fluctuations in the metallic state which give rise to the progressive development of a pseudogap in the spin susceptibility which has been quantitatively analyzed using the Lee-Rice-Anderson theory.

DOI: 10.1103/PhysRevB.90.205132 PACS number(s): 72.15.Nj, 71.20.−b, 73.61.Ph

I. INTRODUCTION

Unconventional superconductors are characterized by the emergence of superconductivity in the vicinity of another ordered state that is a density wave or an (anti)ferromagnetic phase. As far as charge density wave (CDW) is concerned, its discovery under large magnetic fields [1,2] and at zero field [3,4] in the cuprates might indicate that it could play a key role in understanding the high temperature superconductivity. This topic has also been considered in various chalcogenide materials [5–7]. Very recently, a high pressure x-ray study [8] of $TiSe_2$ has demonstrated that the CDW state vanishes at a critical point corresponding to a pressure larger than those for which superconductivity is achieved. This requires one to reinvestigate other materials where superconductivity competes with CDW. In molecular conductors, competition between superconductivity [9] and CDW [10] has been first observed 30 years ago in pressurized (BEDT-TTF)$_2$ReO$_4$ where the maximal critical temperature T_c is about 1.5 K. The transition-metal Ni(dmit)$_2$ -based compounds (dmit is 1,3-dithia-2-thione-4,5 dithiolato; M = Ni, Pd) provide large critical temperatures for quasi-one-dimensional (1D) materials of 6.5 K at $P = 20$ kbar in TTF[Pd(dmit)$_2$]$_2$ [11] or 1.6 K at $P = 7.5$ kbar in TTF[Ni(dmit)$_2$]$_2$ [12,13], both in competition with a CDW ground state. Contrary to most molecular solids, this family is characterized by a small M(dmit)$_2$ highest occupied molecular orbital and lowest unoccupied molecular orbital (HOMO-LUMO) energy difference which leads to a contribution at the Fermi level of both orbitals of the acceptor as evidenced by early band structure calculations [14]. Therefore, the multisheet Fermi surface may induce many phase transitions and a very rich physics with many ground states in competition [15].

More precisely, TTF[Ni(dmit)$_2$]$_2$ is built from alternating TTF chains and Ni(dmit)$_2$ chains stacked along the b axis [16] (see Fig. 1). At ambient pressure, x-ray diffuse scattering experiments have shown the existence of diffuse lines below room temperature which are characteristic of 1D CDW fluctuations along the stacking direction b with the wave vector $q_1 = 0.40(2)b^*$ [17]. They also revealed the existence of possible successive CDW transitions in TTF[Ni(dmit)$_2$]$_2$ below about 50 K. However, the conductivity along the chains exhibits a metallic behavior down to the lowest temperatures without any anomaly which would be expected for a decrease in the density of states at the Fermi level resulting from the opening of a gap [13]. Upon applying pressure, longitudinal resistivity experiments exhibit weak localization at low temperature for pressures lower than $P_{c1} = 5$ kbar and superconductivity appears at about 4 kbar. The superconducting critical temperature is weakly pressure dependent above P_{c1} with $T_c \approx 1.6$ K. Therefore, the commonly accepted experimental image of TTF[Ni(dmit)$_2$]$_2$ pressure-temperature phase diagram [13] resembles that observed in most compounds where superconductivity emerges at the end point of a CDW as in several chalcogenides such as $NbSe_3$ [18], $TiSe_2$ under pressure, and copper doped $TiSe_2$ at ambient pressure [19], or in other molecular conductors such as Per$_2$[Au(mnt)$_2$] [20].

In this paper, we revisit experimentally the pressure-temperature phase diagram of the multiband conductor TTF[Ni(dmit)$_2$]$_2$. We first present longitudinal and transverse resistivity measurements under pressure and spin susceptibility at ambient pressure. This will allow one to draw a new pressure-temperature phase diagram which differs significantly from the already published one [13]. The interpretation

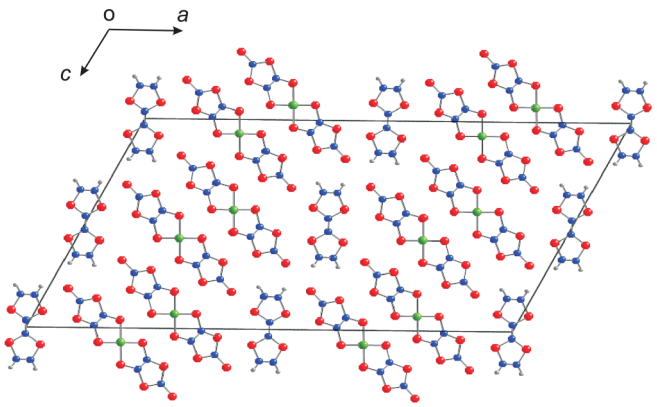

FIG. 1. (Color online) Projection view along the b axis of the TTF[Ni(dmit)$_2$]$_2$ crystal structure. Blue, red, green, and gray balls refer to C, S, Ni, and H atoms, respectively.

of the data will be supported by an electronic structure study by means of first-principles DFT calculations which, by treating both TTF and Ni(dmit)$_2$ in the same way, provide a consistent view of the band structure, charge transfer, and Fermi surface for this multiband molecular conductor. At ambient pressure, the abnormal metallic state with the development of a pseudogap is clearly identified and furthermore, we can quantitatively account for its thermal evolution using the Lee-Rice-Anderson theory [21] in a wide temperature range between 50 and 300 K. In contrast with most systems, our study is able to identify various CDW states, to ascribe the CDWs to peculiar bands and to describe very precisely the evolution of the CDW as a function of temperature and pressure, even in the presence of superconductivity at low temperature. At large pressures, a peak of the CDW transition temperature is also observed, which recalls the behavior of the pressurized TTF-TCNQ compound [22].

II. METHODS

All the measurements have been performed on needle-shaped crystals of TTF[Ni(dmit)$_2$]$_2$ elongated along the b crystallographic axis. For longitudinal resistivity, $\rho_{\parallel}$ measurements, four ring gold pads contacts aligned along the sample were evaporated on the surface before attaching gold wires with silver paste. The typical size of the samples used for these experiments was $0.1 \times 2 \times 0.005$ mm^3 along the a, b, and c directions, respectively. Indeed, we have noted that measuring the longitudinal resistivity is possible only on the thinnest samples to avoid a transverse contribution to the resistivity. For transverse resistivity measurements, the strong needle character and the tendency of getting several crystalline domains upon increasing the thickness of the samples render difficult the determination of the precise injection of the current (a or c directions). Therefore, we simply note $\rho_{\perp}$ the transverse resistivity as we believe that both a and c components of the resistivity tensor contribute in thicker samples that are needed due to the extreme brittleness of the needles. The typical sizes of the samples used here were $0.09 \times 2.1 \times 0.15$ mm^3 along the a, b, and c directions, respectively. For both directions, the applied current was in the range 1–10 μA and the voltage was obtained using a standard low frequency lock-in detection. These transport measurements were performed down to 2 K using a variable temperature insert.

Hydrostatic pressures up to 11 and 30 kbar were generated in a Be-Cu and a Ni-Cr-Al clamped cell, respectively, with Daphne 7373 silicon oil as the pressure transmitting medium. The pressure was measured at room temperature using a manganine gauge and low temperature pressure was corrected as follows: 2 kbar were subtracted for pressures between 2 and 10 kbar, 1.5 kbar for pressures between 11 and 14.5 kbar, and 1 kbar between 15 and 21 kbar. Above 21 kbar, no pressure correction was applied since the oil is already frozen at room temperature [23].

The susceptibility measurements were performed with a superconducting quantum interference device (SQUID) magnetometer. Black and shiny needle-type crystals were carefully chosen and deposited on a flat square silicon sample holder. We were able to have a total weight of 2.51 mg of TTF[Ni(dmit)$_2$]$_2$ needles mounted in parallel with their b axis perpendicular to the magnetic field [which is approximately directed in the planes of the TTF and Ni(dmit)$_2$]. In order to obtain the molar susceptibility of TTF[Ni(dmit)$_2$]$_2$, χ_{measured}, we measured the magnetization of the TTF[Ni(dmit)$_2$]$_2$ needles versus temperature at a magnetic field of 5 T, and subtracted the holder signal measured in the same conditions. Then, the diamagnetic contribution of TTF[Ni(dmit)$_2$]$_2$, $\chi_{\text{dia}} = -5.02 \times 10^{-4}$ cgs/mol [24] was also subtracted. Special care was also taken to well pump the experimental chamber to prevent any presence of oxygen which could give a jump of χ below $\approx$46 K.

The electronic structure calculations were carried out using a numerical atomic orbital density functional theory (DFT) approach [25,26], which was developed for efficient calculations in large systems and implemented in the SIESTA code [27–30]. We have used the generalized gradient approximation to DFT and, in particular, the functional of Perdew, Burke, and Ernzerhof [31]. Only the valence electrons are considered in the calculation, with the core being replaced by norm-conserving scalar relativistic pseudopotentials [32] factorized in the Kleinman-Bylander form [33]. We have used a split-valence double-ζ basis set including polarization orbitals with an energy shift of 10 meV for all atoms [34]. This kind of calculation has been very successful in previous studies of the electronic structure of molecular conductors [35–37]. The energy cutoff of the real space integration mesh was 250 Ry. The Brillouin zone was sampled using a grid of $(3 \times 55 \times 3)$ k points [38] in the irreducible part of the Brillouin zone for determination of density matrix. The results are well converged with respect to the Brillouin zone sampling, real space grid, and range of the atomic orbitals. The x-ray crystal structures determined at 298, 150, and 12 K were used in the calculations [39].

III. RESULTS

A. Electrical conductivity

First, we present the longitudinal and transverse resistivity data that will define the main lines of the phase diagram. At room temperature (RT) and ambient pressure, the longitudinal

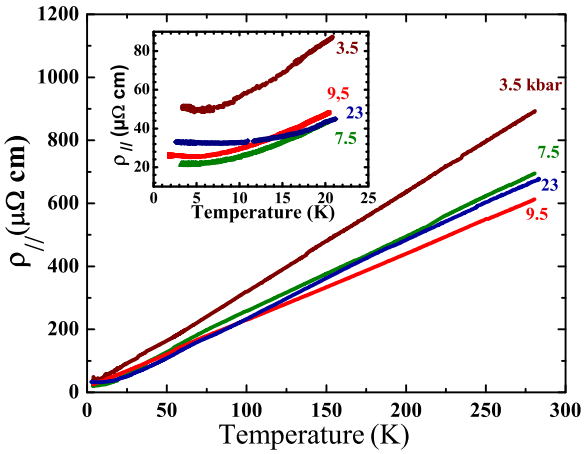

FIG. 2. (Color online) Longitudinal resistivity of TTF[Ni(dmit)$_2$]$_2$ as a function of temperature for various pressures measured on sample 1 and sample 2 at 23 kbar. Inset: zoom of the resistivity versus temperature curves for $T < 25$ K.

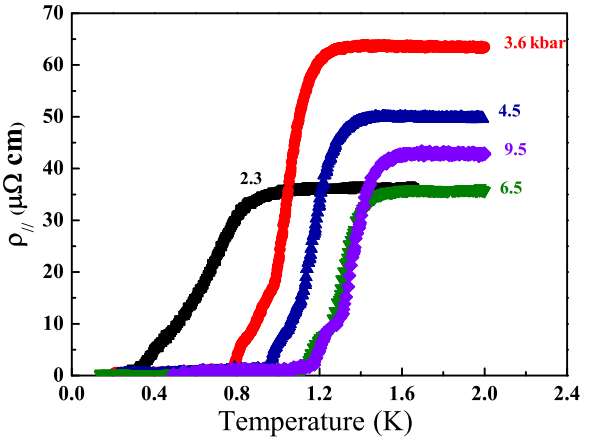

FIG. 3. (Color online) Longitudinal resistivity of TTF [Ni(dmit)$_2$]$_2$ at low temperatures for various pressures.

conductivity obtained along the b axis, $\sigma_{\parallel,\mathrm{RT}} \approx 400\ \Omega^{-1}\,\mathrm{cm}^{-1}$ is in agreement with previous experiments [12,13,16]. It is similar to values measured in other quasi-1D organic conductors such as TTF-TCNQ [40–42] or (TMTSF)$_2$PF$_6$ [43]. The value of the transverse conductivity is $\sigma_{\perp,\mathrm{RT}} \approx 10\ \Omega^{-1}\,\mathrm{cm}^{-1}$ which leads to an anisotropy $\sigma_{\parallel,\mathrm{RT}}/\sigma_{\perp,\mathrm{RT}} \approx 40$. This value is quite small and suggests that the "transverse conductivity" is dominated by the conductivity between alike molecules along c. Indeed, in TTF-TCNQ [40], the ratio between the conductivity along the intermediate conduction axis and $\sigma_{\parallel}$ is about 100 and in (TMTSF)$_2$PF$_6$, this ratio [44–46] is larger than 50, a value far below the typical value of 10^3–10^4 for the ratio of the conductivities along the best and worst conduction axes. Upon increasing the pressure, both longitudinal and transverse conductivities increase with a strong tendency of saturation at the largest pressures typically above 15 kbar for $\sigma_{\parallel}$ and 25 kbar for $\sigma_{\perp}$. At the lowest pressures, the pressure dependence of the longitudinal conductivity is linear with a slope $[\sigma_{\parallel,\mathrm{RT}}(P) - \sigma_{\parallel,\mathrm{RT}}(1\ \mathrm{bar})]/\sigma_{\parallel,\mathrm{RT}}(1\mathrm{bar})$ which varies from 15 to 60%/kbar depending on the sample with an average of 30%/kbar. This value compares well to previous experiments [13] in TTF[Ni(dmit)$_2$]$_2$ and to the (TMTTF)$_2X$ and (TMTSF)$_2X$ families in the metallic regime [45] or a recent study of the o-(DMTTF)$_2X$ family [47]. Finally, the low pressure evolution of the transverse conductivity $[\sigma_{\perp,\mathrm{RT}}(P) - \sigma_{\perp,\mathrm{RT}}(1\ \mathrm{bar})]/\sigma_{\perp,\mathrm{RT}}(1\ \mathrm{bar})$ is typically of the order of 20%/kbar, a value also comparable to the (TMTTF)$_2X$ and (TMTSF)$_2X$ families where this ratio is about 30%–40%/kbar [45].

Figure 2 presents the longitudinal resistivity $\rho_{\parallel}$ as a function of temperature for different pressures measured on samples 1 (low pressure) and 2 (high pressure). At all pressures, $\rho_{\parallel}(T)$ decreases almost linearly with temperature down to 20–30 K. Below this temperature, a quadratic dependence is achieved. Below 6–8 K, a very small localization is observed which disappears above 5 kbar. At high pressure, the low temperature evolution is unclear and a small localization is also observed. However, the brittleness of the samples may lead to the formation of possible cracks in the sample, inducing a weak increase of the resistivity. Figure 3 presents the temperature evolution of the longitudinal resistivity measured on a third sample at the lowest temperatures emphasizing the existence of a superconducting state above $\approx$3 kbar. All these observations are in agreement with the previously reported resistivity data [11].

Figure 4 presents the transverse resistivity $\rho_{\perp}$ as a function of temperature for different pressures. Contrary to the longitudinal resistivity, two clear anomalies are observed at low pressure at temperatures denoted T_{up} and T_{down} ($< T_{\mathrm{up}}$) which are determined as the maxima of the $d(\ln\rho_{\perp})/d(1/T)$ versus $1/T$ curve [inset Fig. 4(a)]. T_{up} remains nearly constant with pressure, $T_{\mathrm{up}} \approx 53$ K, but T_{down} decreases with pressure from

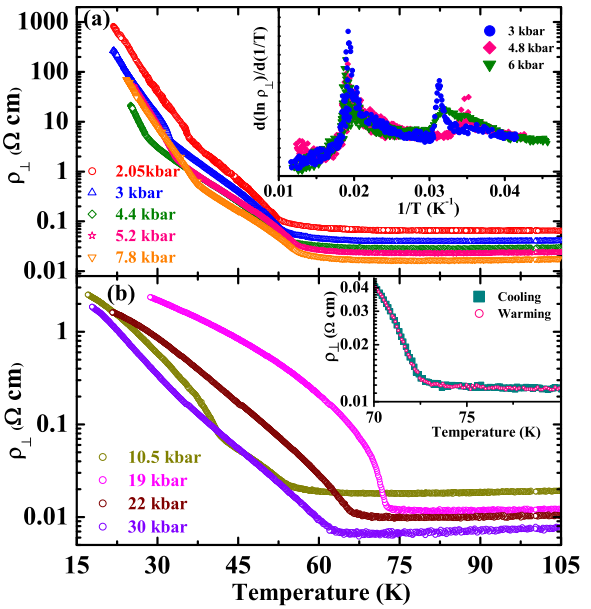

FIG. 4. (Color online) Transverse resistivity of TTF[Ni(dmit)$_2$]$_2$ as a function of temperature for various pressures. (a) At low pressure, measured on sample 2. Inset: $d(\ln\rho_{\perp})/d(1/T)$ versus T curves at different pressures. (b) $\rho_{\perp}(T)$ curves at higher pressure measured on a third sample. Inset: zoom of the $\rho_{\perp}(T)$ measured upon cooling and warming near 70 K at $P = 18$ kbar.

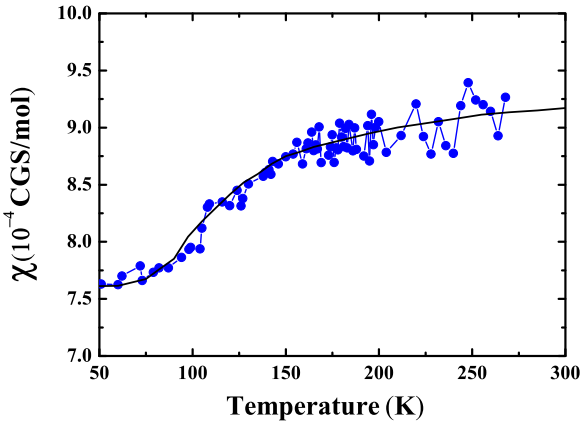

FIG. 5. (Color online) Evolution of the magnetic susceptibility of TTF[Ni(dmit)$_2$]$_2$ as a function of temperature at ambient pressure for $T > 50$ K. The solid line is a fit of the data using the Lee-Rice-Anderson model (see text).

38 K at ambient pressure to 30 K at $P_l = 5$ kbar and then increases up to $P_c \approx 12$ kbar where $T_{down} = T_{up}$. Above this critical pressure, there is only one transition at the temperature T_{up}. It increases strongly with pressure, reaches its maximum of 70 K at $P = 19$ kbar, then decreases again slightly and equals ≈60 K at $P = 30$ kbar. We may add that with such a configuration for the injection of the current, due to a too large resistive background, the superconducting transition cannot be observed at any pressure.

B. Susceptibility

Figure 5 presents the spin susceptibility of TTF[Ni(dmit)$_2$]$_2$ from 50 K to room temperature at ambient pressure. A strong depression of the susceptibility is observed in this temperature range below about 150 K. Figure 6 presents the susceptibility at lower temperatures performed on another sample. Two clear steps are observed at 55 and 38 K, respectively. Even if the data in the full temperature range resembles that published by Brossard *et al.* [24], the existence of these two transitions was never mentioned before on TTF[Ni(dmit)$_2$]$_2$. As highlighted by the comparison with transverse resistivity data in Fig. 6, the kinks occur at the same temperatures T_{up} and T_{down}, respectively, where the transverse resistivity exhibit anomalies. Therefore, this observation confirms the existence of two successive phase transitions upon cooling.

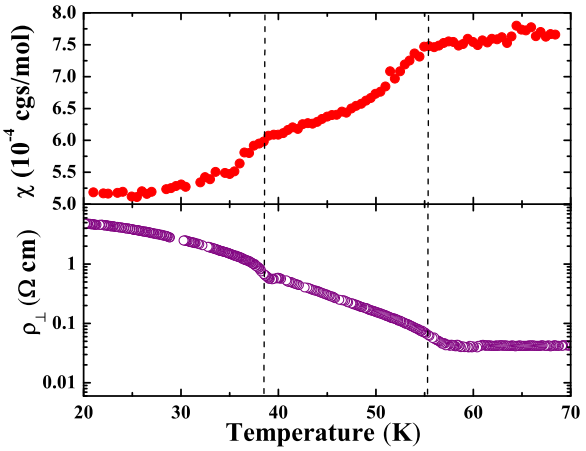

FIG. 6. (Color online) (Top) Evolution of the magnetic susceptibility of TTF[Ni(dmit)$_2$]$_2$ as a function of temperature at ambient pressure. (Bottom) Evolution of the transverse resistivity of TTF[Ni(dmit)$_2$]$_2$ at ambient pressure in the same temperature range. The vertical dashed lines are guides to the eyes.

C. Electronic structure

In order to explain the striking data presented above, a new calculation of the electronic structure will now be presented. Our study of the band structure and Fermi surface as a function of temperature has been carried out on the basis of the centered unit cell containing four TTF and eight Ni(dmit)$_2$ molecules (see Fig. 1).

1. Nature of the band structure

The calculated band structure near the Fermi level at 150 K is shown in Fig. 7. The upper set of bands contains eight bands which slightly split into two groups of four bands each near the Γ point. These bands are mostly built from the LUMO of Ni(dmit)$_2$. Below there is a set of four bands which are based on the HOMO of TTF. Just below there is a set of four bands which are based on the HOMO of Ni(dmit)$_2$. In the following we will refer to these bands as HOMO$_I$. All these bands are cut by the Fermi level only along the b^* direction, i.e., the chains direction, so that they will lead to open lines perpendicular to b^* in the Fermi surface. The lower set of partially filled bands is also made up of four bands based on the Ni(dmit)$_2$ HOMO. However, these bands are cut by the Fermi level in both the b^* and c^* directions and they will lead to closed portions of the Fermi surface. We will refer to these bands as HOMO$_{II}$. As is clear from Fig. 7, the four sets of bands are well separated in the region of the Fermi level and only 0.35 eV below they interact. Looking at the different bands in the region of Γ one can notice that whereas the TTF bands are practically noninteracting, the LUMO bands exhibit a slight but non-negligible interaction,

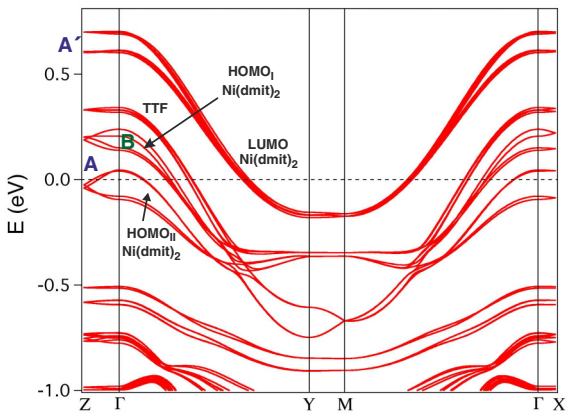

FIG. 7. (Color online) Calculated band structure for TTF[Ni(dmit)$_2$]$_2$ at 150 K. The energy zero corresponds to the Fermi level. $\Gamma = (0,0,0)$, $X = (1/2,0,0)$, $Y = (0,1/2,0)$, $Z = (0,0,1/2)$, and $M = (0,1/2,1/2)$ in units of the monoclinic reciprocal lattice vectors.

whereas the HOMO bands clearly interact and, at least the $HOMO_{II}$ ones, lose the 1D character. We will come back to this later.

In principle, since TTF acts as a donor and $Ni(dmit)_2$ as an acceptor, only the HOMO of TTF and the LUMO of $Ni(dmit)_2$ should be partially filled. However, because of the relatively small energy separation between the HOMO and the LUMO bands of $Ni(dmit)_2$ (i.e., smaller than the band dispersion), the bottom part of the LUMO bands overlaps with the top portion of the HOMO bands. Consequently, in addition to the usual electron transfer between the donor (TTF) and acceptor [$Ni(dmit)_2$ LUMO] bands, there is a second, internal electron transfer, between the HOMO and LUMO bands of $Ni(dmit)_2$. Thus, the present first-principles calculations completely substantiate the so-called *two-band* scenario for this solid [14,48,49]. The calculated band structures at 298 and 12 K are qualitatively similar and thus are not shown here. However, it is clear from the discussion above that this is a quite complex system and, since thermal contraction is not expected to have exactly the same influence over the four sets of bands, the thermal evolution of the different k_F values are not easy to predict without detailed calculations.

2. Band structure parameters versus temperature

The main parameters of the band structure calculated at 298, 150, and 12 K of interest for the present study are summarized in Table I. Using the values in this table, it is possible to calculate the charges associated with TTF, $Ni(dmit)_2$, $Ni(dmit)_2^{LUMO}$, $Ni(dmit)_2^{HOMO_I}$, and $Ni(dmit)_2^{HOMO_{II}}$, as a function of temperature (see Table II). Analysis of these results leads to the following conclusions. First, it is remarkable how the TTF charge remains almost constant with temperature and very similar to the value proposed on the basis of previous Raman studies $\sim+0.80$ [50]. Second, even if the total charge of TTF and $Ni(dmit)_2$ remains almost constant, there is an important electronic rearrangement within $Ni(dmit)_2$ as a function of temperature. For instance, the occupation of the LUMO bands increases while that of the HOMO bands decreases when the temperature is lowered. The emptying of the $HOMO_I$ bands is faster than that of the $HOMO_{II}$ ones. Third, because of this internal electronic redistribution, the Fermi surface associated with the $Ni(dmit)_2$ bands will undergo large changes, whereas that associated with TTF will remain practically constant.

TABLE I. Parameters of the band structure related to the occupation of the partially filled bands of $TTF[Ni(dmit)_2]_2$ at 298, 150, and 12 K. $x^{HOMO_{II}}$ is the number of holes associated with the full set of $HOMO_{II}$ bands, $x^{HOMO_{II}} = 16 - 4(4k_F^{TTF}) + 8(4k_F^{LUMO}) + 4(4k_F^{HOMO_I})$. The $2k_F$ wave vectors of this table (in units of b^*) link $-k_F$ to $+k_F$ through the Γ point and are related to the holes in the quasi-1D bands of Fig. 7.

	298 K	150 K	12 K
$2k_F^{LUMO}$	0.701	0.661	0.643
$2k_F^{TTF}$	0.368	0.373	0.362
$2k_F^{HOMO_I}$	0.224	0.276	0.287
$x^{HOMO_{II}}$	0.048	0.232	0.520

TABLE II. Charges associated with TTF, $Ni(dmit)_2$, $Ni(dmit)_2^{LUMO}$, $Ni(dmit)_2^{HOMO_I}$, and $Ni(dmit)_2^{HOMO_{II}}$ calculated for $TTF[Ni(dmit)_2]_2$ at 298, 150 and 12 K.

	298 K	150 K	12 K
TTF	+0.738	+0.746	+0.724
$Ni(dmit)_2$	−0.368	−0.373	−0.362
Average charge of $Ni(dmit)_2$ due to the LUMO bands	−0.598	−0.678	−0.714
Average charge of $Ni(dmit)_2$ due to all HOMO bands	+0.230	+0.305	+0.352
Average charge of $Ni(dmit)_2$ due to the $HOMO_I$ bands	+0.224	+0.276	+0.287
Average charge of $Ni(dmit)_2$ due to the $HOMO_{II}$ bands	+0.006	+0.029	+0.065

3. Fermi surface versus temperature

The calculated Fermi surfaces for $TTF[Ni(dmit)_2]_2$ at 298, 150, and 12 K are shown in Fig. 8. We only report the (b^*,c^*) section because of the absence of practically any noticeable dispersion in the interlayer direction. Except for the portion associated with the $HOMO_{II}$ bands, all contributions are strongly 1D. As expected, the TTF portion remains unaltered, whereas the LUMO and $HOMO_I$ contributions move in opposite directions when temperature decreases. The $(1–2k_F^{LUMO})$ value, associated to the electron filling of the LUMO band, increases from 0.30 (298 K) to 0.34 (150 K) and 0.36 (12 K), clearly showing the tendency towards the 0.40(2) value of the q_1 x-ray diffuse scattering [17]. Note also

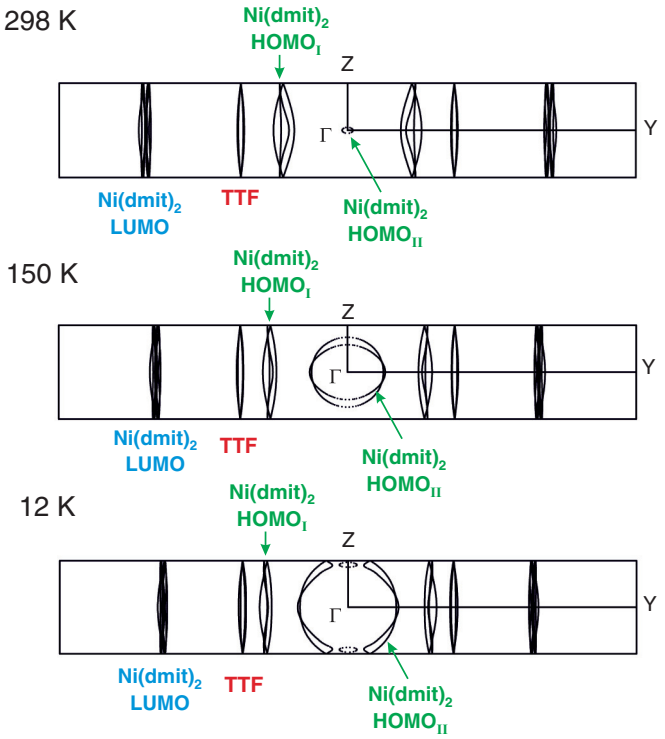

FIG. 8. (Color online) Calculated Fermi surface for TTF $[Ni(dmit)_2]_2$ at 298 K (a), 150 K (b), and 12 K (c).

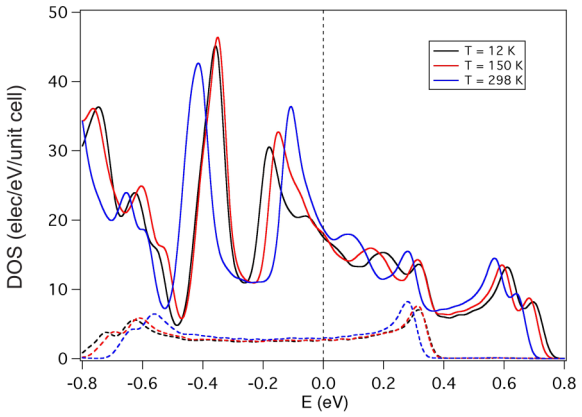

FIG. 9. (Color online) Projected densities of states (elec/eV/unit cell) associated with the TTF (dashed lines) and Ni(dmit)$_2$ (continuous lines) components of TTF[Ni(dmit)$_2$]$_2$ at 298, 150, and 12 K.

that the $2k_F^{\mathrm{HOMO_I}}$ value is also close to the intrastack wave vector 0.22(3) of the q_2 additional diffuse spots detected by x-ray diffuse scattering measurements [17]. This is remarkable since the theoretical description of the charge transfer in molecular conductors where both partners are associated with a nonintegral charge is notoriously difficult [51]. The variation of the Fermi-surface portions associated with the $\mathrm{HOMO_{II}}$ bands is very strong. The contribution of the two $\mathrm{HOMO_{II}}$ bands of higher energy, two circles centered at Γ, is practically nil at 298 K but progressively increases when temperature is lowered and, at very low temperature, the area of the circles is large enough to cross the border of the Brillouin zone. Note that the two $\mathrm{HOMO_{II}}$ bands of lower energy give rise to small pockets around the Z point at 12 K (Fig. 8).

4. Density of states at the Fermi level versus temperature

Finally, let us consider the nature of the density of states at the Fermi level, $N(\varepsilon_F)$. The projected densities of states associated with TTF and Ni(dmit)$_2$ are shown in Fig. 9. As was the case of the total charges, the calculated densities of states at the Fermi level exhibit a very small decrease with temperature for both TTF and Ni(dmit)$_2$ despite the strong electronic reorganization. The breakdown of $N(\varepsilon_F)$ into the various contributions is shown in Table III. Note that for Ni(dmit)$_2$, whereas $N(\varepsilon_F)^{\mathrm{LUMO}}$ and $N(\varepsilon_F)^{\mathrm{HOMO_I}}$ exhibit an expected decrease with temperature, $N(\varepsilon_F)^{\mathrm{HOMO_{II}}}$ shows the opposite behavior, leading to an almost constant $N(\varepsilon_F)^{\mathrm{Ni(dmit)_2}}$ [and consequently, $N(\varepsilon_F)^{\mathrm{TTF}}$] value from 150 K down to low temperatures. The total and partial densities of states in Table III for TTF[Ni(dmit)$_2$]$_2$ at 298 K are around 50% larger than those reported in a previous extended Hückel calculation [24], presumably because the electron repulsions are explicitly treated into account in the present calculations.

TABLE III. Analysis of the different components of the density of states at the Fermi level, $N(\varepsilon_F)$, calculated for TTF[Ni(dmit)$_2$]$_2$ at 298, 150, and 12 K.

	298 K	150 K	12 K
$N(\varepsilon_F)$ (elec/eV/unit cell)	19.24	17.86	17.77
$N(\varepsilon_F)^{\mathrm{TTF}}$	15.24%	14.86%	14.55%
$N(\varepsilon_F)^{\mathrm{Ni(dmit)_2}}$	84.76%	85.13%	85.44%
$N(\varepsilon_F)^{\mathrm{LUMO}}$	53.35%	46.91%	41.93%
$N(\varepsilon_F)^{\mathrm{HOMO_I}}$	22.72%	18.71%	16.83%
$N(\varepsilon_F)^{\mathrm{HOMO_{II}}}$	8.69%	19.51%	26.68%

IV. DISCUSSION

From all the experimental data shown above, we can plot the new pressure-temperature phase diagram of TTF[Ni(dmit)$_2$]$_2$ as shown in Fig. 10. At first sight, this phase diagram mimics that of the well known TTF-TCNQ [22]. However, contrary to TTF-TCNQ, we have here several energy bands associated with the donors and acceptor stacks and TTF[Ni(dmit)$_2$]$_2$ remains metallic at low temperature and exhibits superconductivity. The electronic structure evolution as a function of temperature will help in understanding this phase diagram as cooling is equivalent to increasing the pressure.

In Fig. 10, we have distinguished three different CDW phases ($\mathrm{CDW_1}$, $\mathrm{CDW_2}$, and $\mathrm{CDW_3}$) all coexisting with a metallic phase at low temperature. A possible fourth phase ($\mathrm{CDW_{2'}}$) is mentioned but we have no proof that its symmetry differs from that of the $\mathrm{CDW_2}$ phase. The insulating ground states of these phases are considered to be CDW of the Ni(dmit)$_2$ stacks with different wave vectors assuming that magnetism does not play a role at any pressure as emphasized by the magnetic susceptibility measurements performed at ambient pressure. (Note that an earlier ^{1}H NMR investigation [52] has shown that the TTF stack is not subject to the CDW instability but only to SDW fluctuations). We have also added the superconducting phase, denoted SC, which is stabilized at low temperature in a wide pressure range. In the following, we will first clearly establish the situation at ambient pressure, then discuss the transition temperatures evolution at low pressure ($P < P_c$), and finally, the merging of the two transition

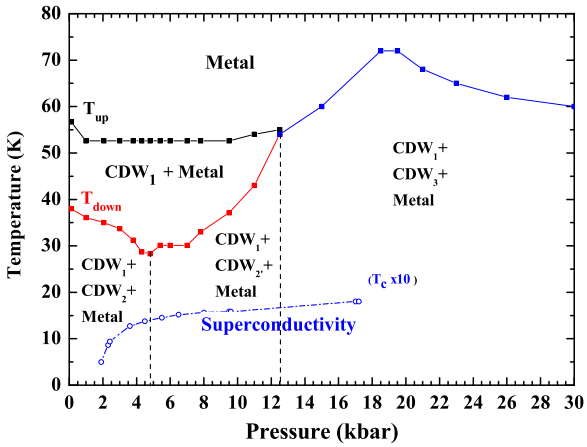

FIG. 10. (Color online) New pressure-temperature phase diagram of TTF[Ni(dmit)$_2$]$_2$. The transition temperatures T_{up} and T_{down} are extracted from transverse resistivity data. The solid and dashed lines are guides for the eyes and separate various regimes. The critical temperature for superconductivity is multiplied by ten to render this phase more visible.

lines into a single one at P_c and its evolution under larger pressures.

A. Ambient pressure phase diagram

As shown above, at ambient pressure, two clear transitions are observed using transverse resistivity and susceptibility measurements. Such a finding is new, so we should first revisit the already known x-ray data [17,48].

1. CDW instabilities

At room temperature, q_1 CDW fluctuations are just appearing so that the mean-field Peierls transition can be considered to be of the order of $T_P^{\rm MF} \approx 300$ K. They appear with the wave vector $q_1 = 0.40(2)b^*$. The CDW correlation length along the chains, $\xi_{q1,\parallel}$, is of the order of b. Upon cooling, this longitudinal correlation length, $\xi_{q1,\parallel}$, extracted from the half width at half maximum of the diffusion lines, increases and becomes very large, $\xi_{q1,\parallel} > 20$ nm at about 55 K, which amounts to $T_{\rm up}$. Nevertheless, from room temperature down to 55 K, there is no interchain CDW correlations. The q_1 CDW interchain correlations develop around 55 K (this crossover temperature amounts to $\approx T_{\rm up}$). Below this temperature, $\xi_{q1,\perp}$ grows and reaches the experimental resolution around 40 K, giving rise to well defined satellite reflections. However, the observation of residual diffuse lines at low temperature shows that the CDW lateral order is not perfect. This lateral order is probably achieved by Coulomb coupling between CDWs. Such a coupling achieves a phase shift of π between CDW located on adjacent stacks and since there are four Ni(dmit)$_2$ stacks along c and two Ni(dmit)$_2$ layers along a, this coupling explains simply the $(0,q_1,0)$ components of the q_1 satellite reflections, similarly to those previously observed in TTF[Pd(dmit)$_2$]$_2$ [17].

We now consider the low temperature CDW fluctuations observed for $q_2 = 0.22(3)b^*$. These quasi-1D CDW fluctuations begin to be detected around 60 K. The x-ray data show that the longitudinal correlation length associated to q_2 increases up to $\xi_{q2,\parallel} \approx 3$ nm ($\approx 8b$) at $T = 30$ K and saturates below this temperature. The inverse of $\xi_{q2,\parallel}$ nicely corresponds to the size of the pocket (≈ 0.4 nm^{-1}) which remains after the longitudinal nesting by q_2. The q_2 CDW fluctuations develop short-range interchain correlations connecting first neighboring chains around 35 K: $\xi_{q2,\perp} \approx 0.7$ nm $\approx c/4$. These correlations always remain local so the quasi-1D diffuse scattering never condensates into well defined satellite reflections. This crossover temperature of about 35 K amounts to $\approx T_{\rm down}$. Finally, the $q_3 = 0.18(3)b^* = q_1 - q_2$ quasi-1D scattering feature should correspond to the intermodulation of the q_1 and q_2 CDWs located on the same Ni(dmit)$_2$ stack. In the presence of such a process one expects to similarly observe a quasi-1D scattering at the $q_1 + q_2$ wave vector. Unfortunately, since within experimental error bars, one has $q_1 + q_2 = b^* - q_1$, this scattering should superimpose to the q_1 CDW scattering.

2. Pseudogap in the density of states

TTF[Ni(dmit)$_2$]$_2$ is a quasi-1D material with uncorrelated spins on the Ni(dmit)$_2$ stacks. As a result, upon cooling, any anomaly in the temperature evolution of the spin susceptibility is the signature of a reduction of the density of states. The effect of the 1D fluctuations on the density of states has been calculated by Lee-Rice-Anderson [21]. Considering that the experimental fall of the density of states is related to only one bunch of bands of TTF[Ni(dmit)$_2$]$_2$, we were able to fit perfectly the susceptibility data (solid line in Fig. 5) using as the only fitting parameter, its mean-field transition temperature, $T_P^{\rm MF} = 300$ K in excellent agreement with the previous analysis of the x-ray data. Another pseudogap opens at lower temperatures, associated to the q_2 CDW fluctuations. This explains the strong anomaly of the spin susceptibility at $T_{\rm up}$. At $T_{\rm down}$, lateral correlations of q_2 fluctuations accelerate the reduction of the density of states so that the spin susceptibility undergoes a second kink. In addition, we can notice, in Fig. 6, that the loss of susceptibility at $T_{\rm up}$ is nearly twice the loss at $T_{\rm down}$. The total loss of susceptibility between room temperature and 20 K (Figs. 5 and 6) amounts to 4.1×10^{-4} cgs/mol. Considering that the susceptibility is a Pauli one, this corresponds to a loss of density of states of 12.7 (elec/eV/unit cell) which amounts to 72% of the density of states calculated by the DFT method at the medium temperature 150 K. The sum of the DFT density of states of the LUMO and HOMO$_{\rm I}$ amounts to 66% at 150 K. There is a fair agreement between the experimental loss of density of states and the DFT calculation. This qualitatively confirms our scenario that CDW involves successively the LUMO and HOMO$_{\rm I}$ bands. This analysis is also coherent with ^{13}C NMR data [53] where CDW fluctuations have been observed on the Ni(dmit)$_2$ stack at room temperature. Below about 160 K, the steeper decrease of the Knight shift [54], also proportional to the density of states, indicated the further development of the pseudogap.

3. Relation with the electronic structure

One can link these CDW instabilities to the relevant Fermi-surface nesting process. From Table I, one has $1–2k_F^{\rm LUMO} \sim 0.35b^*$ at 50 K which, as mentioned, is close to the experimental value $q_1 = 0.40(2)b^*$. Therefore, the transition at $T_{\rm up}$ is related to the nesting of the LUMOs. Similarly, $2k_F^{\rm HOMO_I} \approx 0.28b^*$ is close to the experimental value, $q_2 = 0.22b^*$. Therefore, the second transition at $T_{\rm down}$, may correspond to the nesting of the HOMO$_{\rm I}$ bands. The absence of any anomaly in the longitudinal resistivity (not shown) either at $T_{\rm up}$ or at $T_{\rm down}$ can now be easily understood: At $T_{\rm up}$, the density of states of the LUMOs is negligible as shown by the susceptibility data, so that its contribution to the conductivity of the sample is also negligible. A similar conclusion can be drawn at $T_{\rm down}$ for the HOMO$_{\rm I}$. The sharp transitions in the transverse resistivity are then the signature of the formation of alternating metallic and insulating (CDW) slabs perpendicular to the current injection direction with the b axis parallel to the domain walls in order to have a metallic longitudinal resistivity. To conclude, TTF[Ni(dmit)$_2$]$_2$ undergoes at ambient pressure two successive CDW transitions (denoted CDW$_1$ and CDW$_2$ in Fig. 10) at $T_{\rm up}$ and $T_{\rm down}$ affecting, respectively, the LUMO and HOMO$_{\rm I}$ bands, as does TTF[Pd(dmit)$_2$]$_2$ at 150 and 105 K [17]. However, in the Pd compound, the 105 K phase transition involves the whole bunch of HOMO bands [14,17], and thus leads to an insulating ground state.

B. Low pressure phase diagram

We now discuss the evolution of the transition temperatures under pressure at low pressures. We will assume that increasing the pressure is equivalent to cooling. Therefore, as shown by the electronic structure calculations, only a small variation of the charge transfer from TTF to the $Ni(dmit)_2$ chains is expected. In contrast, a large internal charge transfer from the HOMOs to the LUMOs in the $Ni(dmit)_2$ chains is also expected (see Table II). This implies an increase of $b^* - 2k_F^{\mathrm{LUMO}} = q_1$ with pressure (Table I). The associated increase of hole density leads to an increase of $2k_F^{\mathrm{HOMO_I}} = q_2$ with pressure (Table I) and a weak modification of the intermodulation wave vector $q_3 = q_1 - q_2$. As shown in Fig. 8, the warping of both LUMO and $\mathrm{HOMO_I}$ Fermi surface, which decreases upon cooling at ambient pressure, is expected to behave similarly upon increasing pressure. The weak increase of T_{up} with pressure is thus the signature of the weak evolution of the warping of the LUMO Fermi surface with pressure. Since the warping of the $\mathrm{HOMO_I}$ bands decreases strongly upon cooling (see Fig. 8), we would expect an increase of T_{down} with pressure which is effectively observed between 5 kbar and P_c. However, this is not the case at low pressure. As a result, either the nesting wave vector changes at 5 kbar leading to a $\mathrm{CDW}_{2'}$ phase different from the low pressure CDW_2 phase or another parameter influences the evolution of the transition temperature, in which case, these two phases correspond to the same nesting vector. The complexity of the $\mathrm{HOMO_I}$ contribution to the Fermi surface, as shown in Fig. 8, suggests that a weak modification of the nesting vector cannot be ruled out due to the simultaneous large increase of T_{up} and T_{down} upon increasing pressure and that the transition between two different CDWs with different wave vectors is possible. With our experimental data, it is not possible to decide which scenario is the most adequate and x-ray or neutron measurements under pressure would be needed to reach a firm conclusion as was the case for TTF-TCNQ [55].

C. High pressure phase diagram

At P_c, the two transition lines merge into a single one. We will now discuss the possible origin of this phenomenon. First, we must remind one that T_{up} corresponds to the nesting of the eight LUMO bands, whereas T_{down} corresponds to the nesting of only four HOMO bands, the $\mathrm{HOMO_I}$ ones. The possible disappearance of either the LUMO-LUMO or the $\mathrm{HOMO_I}$-$\mathrm{HOMO_I}$ nesting at P_c can be ruled out due to the increased nesting conditions upon increasing pressure. The only possibility remaining is to consider an additional LUMO-$\mathrm{HOMO_I}$ nesting. Since this new process involves only four bands, the LUMO-LUMO nesting for the four remaining LUMO bands must still be present. Thus, the stabilization of such a mixed nesting is possible only if the nesting vectors for both processes are nearly identical. If one considers the ambient pressure values, it is found that the LUMO-LUMO nesting wave vector, $b^* - 2k_F^{\mathrm{LUMO}} = q_1 = 0.40(2)b^*$, and the LUMO-$\mathrm{HOMO_I}$ nesting wave vector, $k_F^{\mathrm{LUMO}} + k_F^{\mathrm{HOMO_I}} \cong (0.30 + 0.11)b^* = 0.41(3)b^*$ (denoted q_{av}), are identical within error bars.

The coincidence of the nesting vectors q_1 and q_{av} is optimal at only one pressure or at least in a weak range of pressure. At this optimal pressure, the simultaneous nesting of the LUMO and $\mathrm{HOMO_I}$ bands with the same wave vector (i.e., with the energy cost of a single lattice distortion) provides the best energy gain, so the highest transition temperature for the stabilization of a CDW order. We believe that this is achieved at 19 kbar where a peak in T_{up} is observed. A commensurate nesting would be an alternative scenario occurring at this pressure as observed in TTF-TCNQ [56] or in TSeF-TCNQ [22], where a $b^*/3$ commensurability is observed. For such a $1/3$ commensurability, a first order phase transition is expected to occur at the critical temperature. As shown in Fig. 4, no thermal hysteresis has been observed here weakening the possibility of such a commensurability. In addition, the evolution of q_1 and q_{av} with pressure estimated from the band structure calculation does not exhibit a clear evolution towards "magic" simple commensurate values. Therefore, we propose for the CDW_3 region the following scenario. At 19 kbar one can consider that $q_1 = q_{av}$. For lower and larger pressures, the two wave vectors are nearly identical leading to an averaged $2k_F$ with a modulation of the CDW that will, locally, provide either q_1 or q_{av}. This beating mechanism corresponds to a solitonlike modulation, a mechanism already proposed by Bjelis and Barisic [57] for some transition-metal chalcogenides, and later also used to explain some puzzling experimental observations for the monophosphate tungsten bronze $(PO_2)_4(WO_3)_{2m}$ with alternate stacking of $m = 4$ and $m = 6$ layers [58].

D. The evolution of the electronic structure under pressure

A closer look at the electronic structure calculations also provides support for the proposed mechanism. Looking at the band structure of Fig. 7 it is clear that both the HOMO and LUMO sets of eight bands separate into two subgroups of four bands. Essentially, to increase the one dimensionality of the LUMO and $\mathrm{HOMO_I}$ bands one needs (i) to increase the dispersion in the b^* direction, and (ii) to decrease the separation between the different bands of the same subgroup (i.e., for instance B in Fig. 7 for the $\mathrm{HOMO_I}$ bands). If we assume that the effect of thermal contraction and pressure are analogous, our calculations as a function of temperature provide clear support for the fulfillment of the two conditions. For instance, going from 298 to 12 K, the average dispersion of the LUMO and HOMO bands increases by a factor 1.15–1.20. As clearly shown by the Fermi surfaces of Fig. 8, decreasing the temperature leads to a reduction of the separation between the different components of the LUMO as well as $\mathrm{HOMO_I}$ portions of the Fermi surface, although the effect is stronger for the components of the $\mathrm{HOMO_I}$ subgroup. Thus, we conclude that an increase of pressure most likely drives the system to a situation very favorable for the proposed mechanism to occur. It is important to point out that there are also structural reasons leading credence to this mechanism. Within the $Ni(dmit)_2$ stacks there are three different types of lateral interactions, denoted as I, II, and III in Fig. 11(a). Of course, these lateral interactions are considerably weaker than those along the chains. As has been analyzed elsewhere [14,59], interaction I is approximately five times stronger than interaction II and interaction III is very small. The separation between the

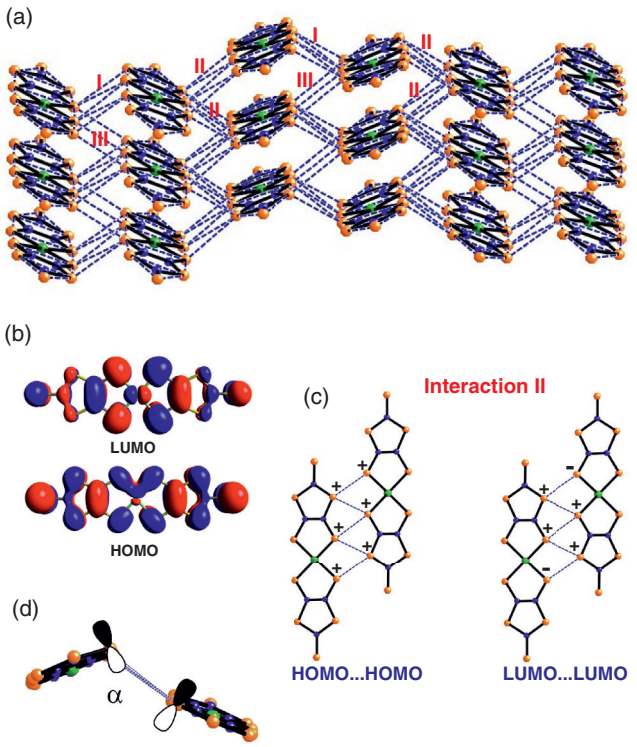

FIG. 11. (Color online) (a) Lateral view of the $Ni(dmit)_2$ stacks where the three different interactions are labeled; (b) HOMO and LUMO of $Ni(dmit)_2$ calculated using the experimental geometry in $TTF[Ni(dmit)_2]_2$; (c) HOMO$\cdots$HOMO and LUMO$\cdots$LUMO interaction II where the S p_z orbitals have simply been represented by a positive or negative sign; and (d) interaction II viewed along a direction parallel to the long axis of the molecules schematically showing that an increase in the angle between the molecular planes leads to a decrease of the orbital overlaps.

different bands of a given subgroup is mostly controlled by interaction II [60]. The HOMO and LUMO of $Ni(dmit)_2$ are shown in Fig. 11(b). In the HOMO, all S p_z contributions in one of the long sides of the molecule have the same sign, whereas in the LUMO there is a sign change in the middle of the molecule. This means that all p_z orbitals of the HOMO contribute to the lateral interaction II [see Fig. 11(c) where every S p_z orbital has simply been represented by a positive or negative sign] which will thus be sizable. In the case of the LUMO, the sign change and the longitudinal shift of one of the molecules lead to a partial cancellation of overlaps [see Fig. 11(c)] so that interaction II is very weak. In other words, interaction II for the LUMO orbitals will always be very weak whatever the actual pressure it is. In contrast, interaction II for the HOMO orbitals will exhibit a pressure dependence via the change in the associated overlap integral. As shown in Fig. 11(d), which is a view of interaction II along a direction parallel to the long molecular axis of the molecules, a slight increase of the angle between the two molecular planes α, which is a most likely consequence of pressure, decreases the strength of the interaction. Consequently, pressure will decrease the separation of the components of the $HOMO_I$ portion of the Fermi surface which thus acquires an even more one-dimensional character. We conclude that both the analogy between the effect of pressure and thermal contraction on the electronic structure and the above analysis of the correlation between the crystal and electronic structure of the $Ni(dmit)_2$ stacks provide support for the proposed mechanism leading to the merging of the two lines in the phase diagram of Fig. 10.

V. CONCLUSION

The pressure-temperature phase diagram of $TTF[Ni(dmit)_2]_2$ has been revisited experimentally using transport and SQUID experiments. A band structure obtained using DFT calculations confirms the multiband character of this compound, with one band associated with the TTF chains and three different types of bands associated with the $Ni(dmit)_2$ chains (LUMO, $HOMO_I$, and $HOMO_{II}$). An analysis based on these three techniques, associated to a reinterpretation of the former x-ray data has allowed one to elucidate this new phase diagram which is puzzling since a superconducting state is stabilized at low temperature even in the presence of several CDW instabilities. The longitudinal conductivity is metallic and dominated by the 2D, $HOMO_{II}$ band at low temperatures. The transverse resistivity presents an insulating behavior at low temperature resulting in a phase coexistence in the sample. At low pressure, a successive nesting of the LUMO and $HOMO_I$ bands is observed upon cooling. Above 12 kbar, only one transition occurs and is attributed to an additional nesting process that is the partial nesting of the LUMO with the $HOMO_I$ portions of the Fermi surface through the Γ point of the Brillouin zone.

In the context of the competition between CDW and superconductivity, which is at this moment the subject of extensive and renewed interest [1–4,8], our study brings new and relevant information. First, in contrast with many other systems where competition between superconductivity and CDW occur, the $TTF[Ni(dmit)_2]_2$ system is a multiband metal in which the acceptor $[Ni(dmit)_2]$ contributes with several and not just one orbital to the band structure. These systems are atypical and more complex than usual single band systems where superconductivity develops beyond a critical point where the CDW ground state vanishes [9,18–20]. Second, the $TTF[Ni(dmit)_2]_2$ system which exhibits a competition between superconductivity and CDW is similar to transition-metal dichalcogenides such as $TiSe_2$ (see Ref. [8], and earlier references therein). However, in contrast with the case of the latter systems, our study is able to ascribe the CDWs to peculiar bands and to describe very precisely the evolution of the CDW as a function of temperature and pressure. In this respect our work provides important keys for the present debate on the competition between CDW and superconductivity in both organic and inorganic systems. Third, the $TTF[Ni(dmit)_2]_2$ system exhibits an abnormal metallic state with the development of a pseudogap, as is the case in the high-T_c superconductors. However, in $TTF[Ni(dmit)_2]_2$, the CDW nature of the order parameter whose fluctuations give rise to the pseudogap is clearly identified and furthermore we can quantitatively account for its thermal evolution using the Lee-Rice-Anderson theory [21]. Here we experimentally verified such a theory on a wide temperature range starting from T_P^{MF} to $T_P^{MF}/5 \approx T_{up}$.

ACKNOWLEDGMENTS

W.K. acknowledges PHC–Utique program CMCU 10G1306 from a France-Tunisia cooperation for partial financial support. The work in Bellaterra and Barcelona was supported by MINECO-Spain (Grants No. CSD2007-00041, No. FIS2012-37549-C05-05, and No. CTQ2011-23862-C02-02), Generalitat de Catalunya (Grants No. 2009 SGR 1459 and No. 2014 SGR 301), and XRQTC. The authors acknowledge C. Bourbonnais for fruitful discussions and S. Charfi-Kaddour for multiple discussions and hints in the interpretation of the data.

[1] T. Wu, H. Mayaffre, S. Krämer, M. Horvatic, C. Berthier, W. N. Hardy, R. Liang, D. A. Bonn, and M. H. Julien, Nature (London) **477**, 191 (2011).

[2] D. LeBoeuf, S. Kramer, W. N. Hardy, R. Liang, D. A. Bonn, and C. Proust, Nat. Phys. **9**, 79 (2012).

[3] R. Comin, A. Frano, M. M. Yee, Y. Yoshida, H. Eisaki, E. Schierle, E. Weschke, R. Sutarto, F. He, A. Soumyanarayanan, Yang He, M. Le Tacon, I. S. Elfimov, Jennifer E. Hoffman, G. A. Sawatzky, B. Keimer, and A. Damascelli, Science **343**, 390 (2014).

[4] E. H. da Silva Neto, P. Aynajian, A. Frano, R. Comin, E. Schierle, E. Weschke, A. Gyenis, J. Wen, J. Schneeloch, Z. Xu, S. Ono, G. Gu, M. Le Tacon, and A. Yazdani, Science **343**, 393 (2014).

[5] J. A. Wilson, F. J. Salvo, and S. Mahajan, Phys. Rev. Lett. **32**, 882 (1974).

[6] R. L. Withers and J. A. Wilson, J. Phys. C: Solid State Phys. **18**, 4809 (1986).

[7] R. H. Friend and A. D. Yoffe, Adv. Phys. **36**, 1 (1987).

[8] Y. I. Joe, X. M. Chen, P. Ghaemi, K. D. Finkelstein, G. A. de la Pena, Y. Gan, J. C. T. Lee, S. Yuan, J. Geck, G. J. MacDougall, T. C. Chaing, S. L. Cooper, E. Fradkin, and P. Abbamonte, Nat. Phys. **10**, 421 (2014).

[9] S. S. P. Parkin, E. M. Engler, R. R. Schumaker, R. Lagier, V. Y. Lee, J. C. Scott, and R. L. Greene, Phys. Rev. Lett. **50**, 270 (1983)

[10] S. Ravy, R. Moret, J. P. Pouget, R. Comès, and S. S. P. Parkin, Phys. Rev. B **33**, 2049 (1986).

[11] L. Brossard, M. Ribault, L. Valade, and P. Cassoux, J. Phys. **50**, 1521 (1989).

[12] L. Brossard, M. Ribault, M. Bousseau, L. Valade, and P. Cassoux, C. R. Acad. Sci. Paris **302**, 205 (1986).

[13] L. Brossard, M. Ribault, L. Valade, and P. Cassoux, Phys. Rev. B **42**, 3935 (1990).

[14] E. Canadell, I. E.-I. Rachidi, S. Ravy, J.-P. Pouget, L. Brossard, and J.-P. Legros, J. Phys. France **50**, R2967 (1989).

[15] R. Kato, Bull. Chem. Soc. Jpn. **87**, 355 (2014).

[16] M. Bousseau, L. Valade, J.-P. Legros, P. Cassoux, M. Garbauskas, and L. V. Interrante, J. Am. Chem. Soc. **108**, 1908 (1986).

[17] S. Ravy, J.-P. Pouget, L. Valade, and J.-P. Legros, Europhys. Lett. **9**, 391 (1989).

[18] A. Briggs, P. Monceau, M. Nunez-Regueiro, J. Peyrard, M. Ribault, and J. Richard, J. Phys. C: Solid State Phys. **13**, 2117 (1980).

[19] A. F. Kusmartseva, B. Sipos, H. Berger, L. Forro, and E. Tutiš, Phys. Rev. Lett. **103**, 236401 (2009).

[20] D. Graf, J. S. Brooks, M. Almeida, J. C. Dias, S. Uji, T. Terashima, and M. Kimata, Europhys. Lett. **85**, 27009 (2009).

[21] P. A. Lee, T. M. Rice, and P. W. Anderson, Phys. Rev. Lett. **31**, 462 (1973).

[22] For a review, see D. Jérome and H. J. Schulz, Adv. Phys. **31**, 299 (1982); **51**, 293 (2002).

[23] K. Yokogawa, K. Murata, H. Yoshino, and S. Aoyama, Jpn. J. Appl. Phys. **46**, 3636 (2007).

[24] L. Brossard, E. Canadell, L. Valade, and P. Cassoux, Phys. Rev. B **47**, 1647(R) (1993).

[25] P. Hohenberg and W. Kohn, Phys. Rev. **136**, B864 (1964).

[26] W. Kohn and L. J. Sham, Phys. Rev. **140**, A1133 (1965).

[27] J. M. Soler, E. Artacho, J. Gale, A. García, J. Junquera, P. Ordejón, and D. Sánchez-Portal, J. Phys.: Condens. Matter **14**, 2745 (2002).

[28] E. Artacho, E. Anglada, O. Dieguez, J. D. Gale, A. García, J. Junquera, R. M. Martin, P. Ordejón, J. M. Pruneda, D. Sánchez-Portal, and J. M. Soler, J. Phys.: Condens. Matter **20**, 064208 (2008).

[29] For more information on the SIESTA code visit http://icmab.cat/leem/siesta/

[30] For a review on applications of the SIESTA approach in materials science, see D. Sánchez-Portal, P. Ordejón, and E. Canadell, *Structure and Bonding*, Vol. 113 (Springer-Verlag, Berlin, Heidelberg, 2004), pp. 103–170.

[31] J. P. Perdew, K. Burke, and M. Ernzerhof, Phys. Rev. Lett. **77**, 3865 (1996).

[32] N. Troullier and J. L. Martins, Phys. Rev. B **43**, 1993 (1991).

[33] L. Kleinman and D. M. Bylander, Phys. Rev. Lett. **48**, 1425 (1982).

[34] E. Artacho, D. Sánchez-Portal, P. Ordejón, A. García, and J. M. Soler, Phys. Status Solidi B **215**, 809 (1999).

[35] P. Foury-Leylekian, J.-P. Pouget, Y.-J. Lee, R. M. Nieminen, P. Ordejón, and E. Canadell, Phys. Rev. B **82**, 134116 (2010).

[36] P. Auban-Senzier, D. Jérome, N. Doiron-Leyraud, S. René de Cotret, A. Sedeki, C. Bourbonnais, L. Taillefer, P. Alemany, E. Canadell, and K. Bechgaard, J. Phys.: Condens. Matter **23**, 345702 (2011).

[37] P. Alemany, J.-P. Pouget, and E. Canadell, Phys. Rev. B **85**, 195118 (2012).

[38] H. J. Monkhorst and J. D. Pack, Phys. Rev. B **13**, 5188 (1976).

[39] S. Hebrard-Bracchetti, Ph.D. thesis, Université de Bordeaux I, 1996.

[40] J. Cohen, L. B. Coleman, A. F. Garito, and A. J. Heeger, Phys. Rev. B **10**, 1298 (1974).

[41] J. P. Ferraris and T. F. Finnegan, Solid State Commun. **18**, 1169 (1976).

[42] J. R. Cooper, D. Jérome, S. Etemad, and E. M. Engler, Solid State Commun. **22**, 257 (1977).

[43] K. Bechgaard, C. S. Jacobsen, K. Mortensen, H. J. Pedersen, and N. Thorup, Solid State Commun. **33**, 1119 (1980).

[44] R. L. Greene and E. M. Engler, Phys. Rev. Lett. **45**, 1587 (1980).

[45] J. Moser, M. Gabay, P. Auban-Senzier, D. Jérome, K. Bechgaard, and J. M. Fabre, Eur. Phys. J. B **1**, 39 (1998).

[46] M. Dressel, K. Petukhov, B. Salameh, P. Zornoza, and T. Giamarchi, Phys. Rev. B **71**, 075104 (2005).
[47] P. Foury-Leylekian, P. Auban-Senzier, C. Coulon, O. Jeannin, M. Fourmigué, C. Pasquier, and J.-P. Pouget, Phys. Rev. B **84**, 195134 (2011).
[48] S. Ravy, E. Canadell, and J.-P. Pouget, in *The Physics and Chemistry of Organic Superconductors*, edited by G. Saito and S. Kagoshima (Springer-Verlag, Berlin, 1989), p. 252.
[49] E. Canadell, S. Ravy, J.-P. Pouget, and L. Brossard, Solid State Commun. **75**, 633 (1990).
[50] K. I. Pokhodnya, C. Faulmann, I. Malfant, R. Andreu-Solano, P. Cassoux, A. Mlayah, D. Smirnov, and J. Leotin, Synth. Met. **103**, 2016 (1999).
[51] J. Fraxedas, Y. J. Lee, I. Jiménez, R. Gago, R. M. Nieminen, P. Oredejón, and E. Canadell, Phys. Rev. B **68**, 195115 (2003).
[52] C. Bourbonnais, P. Wzietek, D. Jérome, F. Creuzet, L. Valade, and P. Cassoux, Europhys. Lett. **6**, 177 (1988).
[53] A. Vainrub, E. Canadell, D. Jérome, P. Bernier, T. Nunes, M.-F. Bruniquel, and P. Cassoux, J. Phys. France **51**, 2465 (1990).
[54] A. Vainrub, D. Jérome, M.-F. Bruniquel, and P. Cassoux, Europhys. Lett. **12**, 267 (1990).
[55] S. Megtert, R. Comès, C. Vettier, R. Pynn, and A. F. Garito, Solid State Commun. **31**, 977 (1979); **37**, 875 (1981).
[56] R. H. Friend, M. Miljak, and D. Jérome, Phys. Rev. Lett. **40**, 1048 (1978).
[57] A. Bjelis and S. Barisic, J. Phys. C **19**, 5607 (1986).
[58] P. Foury-Leylekian, E. Sandré, S. Ravy, J.-P. Pouget, E. Elkaim, P. Roussel, D. Groult, and Ph. Labbé, Phys. Rev. B **66**, 075116 (2002).
[59] M.-L. Doublet, Ph.D. thesis, Université Paris-Sud, Orsay, France, 1994.
[60] Interaction I controls the average separation between the two subgroups of four bands within both the LUMO and HOMO bunches of bands (i.e., see A and A' in Fig. 7).